

# Cathodoluminescence Studies of Defects in Coated Boron Nitride

Kévin Guerch<sup>1,2,3</sup>, Justin Dekany<sup>2</sup>, JR Dennison<sup>2</sup>, Justin Christensen<sup>2</sup>, Thierry Paulmier<sup>1</sup>,  
Sophie Guillemet-Fritsch<sup>3</sup>, Pascal Lenormand<sup>3</sup>

<sup>1</sup> ONERA, 2 avenue Edouard Belin 31055 Toulouse Cedex 4 – France

<sup>2</sup> **Materials Physics Group**, Physics Department, Utah State University, Logan, UT 84322 – United-States

<sup>3</sup> **CIRIMAT**, Université de Toulouse, CNRS, UPS, 118 route de Narbonne 31062 Toulouse cedex 09 – France

jr.dennison@usu.edu, thierry.paulmier@onera.fr

## Abstract

Optical emission properties of Boron Nitride (BN) substrates, BN with alumina (Al<sub>2</sub>O<sub>3</sub>) coating, and thermally-annealed alumina-coated boron nitride (an-BN/Al<sub>2</sub>O<sub>3</sub>) were investigated under electron irradiation using cathodoluminescence (CL) measurements. Tests were performed temperatures ranging from ~100 K to ~300 K, with monoenergetic beams from 5 keV to 30 keV, and electron flux densities from 1 nA.cm<sup>-2</sup> to 500 nA.cm<sup>-2</sup>. These experiments were conducted to identify the effects of coating and thermal annealing on the nature and occupation of defect states in different samples with BN substrates. Previous studies have shown that these treatments can limit the charging of BN substrates. Consequently, thorough investigations of electron trapping and recombination processes as a function of low temperature, dose and charging/discharge were performed in order to explain the differences of electrical behaviour and compare the CL spectra of the three different samples studied. Broad features associated with the BN and sharper features resulting from the annealed alumina coating were observed. Changes in the intensity, energy, and width of the features with sample treatments were observed. Different incident beam parameters were used to associate these features with specific types of defect states. The effects of charging, temperature- and dose-dependent conductivity, and thermal annealing and aging of the samples on the CL spectra were investigated. These were used to study defect creation and occupation and to understand the predominant physical mechanisms and main structural and chemical differences between these ceramic configurations.

**Keywords:** aluminium oxide, annealing, boron nitride, cathodoluminescence, ceramics, charging, coating, defects, electron irradiation

## Introduction

Technical ceramic materials are subjected to extreme conditions in plasma environments, such as those encountered by satellites in space [1], devices for plasma vapour deposition [2], high power applications [3], or nuclear radiation [4]. To survive, these ceramic insulators must have exceptional electrical and thermal properties. Boron nitride (BN) is used in particular because it combines good electrical insulation and high thermal conductivity [5]. However, partially shielded environments such as those found in spacecraft interiors irradiated by electrons with preferentially higher energies can lead to charge trapping in the ceramic's bulk. With the aim to limit charging of BN under electron irradiation, studies of a coating and a thermal treatment of this substrate were performed. Specifically, BN substrates were coated with alumina ( $\text{Al}_2\text{O}_3$ ) coatings (using plasma vapour deposition) with some coated BN subsequently subjected to thermal annealing under vacuum.

This study focuses on the nature, density and occupation of the localised defects (traps), which control electrical and optical behaviour in these systems. These traps are generated from physical (*e.g.*, vacancies, interstitial, or grain boundaries) and chemical (*e.g.*, substitutional or interstitial impurities) defects in the crystallographic phase of materials. Trap depths (*i.e.*, the binding energies of trapped charges) depend on the nature of the defects. Simple band theory of disordered materials, based on the energy and spatial distributions of these deep trap (DT) defect states, is used to describe the dark conductivity and radiation induced conductivity (RIC) [6] and the electron beam-induced optical emission (cathodoluminescence) spectra.

On one hand, we compare the nature and densities of defects of BN substrates, alumina-coated BN (BN/ $\text{Al}_2\text{O}_3$ ), and annealed  $\text{Al}_2\text{O}_3$ -coated BN (an-BN/ $\text{Al}_2\text{O}_3$ ) through studies of the energies and intensities of spectral features of emitted light. On the other hand, we investigate the significant influence of thermal annealing and extended radiation doses (aging) experienced by the materials on charge trapping processes, trap creation and annihilation, electron release kinetics, and charge mobility. The sample temperature during irradiation tests has a substantial influence on electron transport and optical spectra through the electron transitions in the band gap of an-BN/ $\text{Al}_2\text{O}_3$ . These, in turn, are related to the charging/discharge processes and especially to the sample surface deterioration as a function of time and thus of dose.

## Experimentation

The ultrahigh vacuum Electron Emission Test (EET) chamber at Utah State University [7], [8] was used to investigate the cathodoluminescence (CL) of the ceramic samples. Figure 1 provides a schematic overview of instrumentation used during the tests described herein. This versatile facility allows the characterization of spacecraft materials in different representative space conditions. Ultrahigh vacuum ( $\sim 1.10^{-6}$  Pa) is achieved through use of mechanical, turbomolecular and ion pumps. For most tests, samples were mounted on a carousel held at room temperature which has ten sample holder faces and one location for a Faraday cup used to monitor incident beam profiles and fluxes. Low temperature tests from  $\sim 100$  K up to  $\sim 300$  K were made using a cryogenic sample holder [9], using a closed-cycle He refrigerator installed on a flange of the chamber. A high-energy electron gun (Kimball, Model EGPS-21B) provided an electron beam with incident energies of 5 keV to 30 keV (5, 10, 15, 20, 25 and 30 keV  $\pm 0.1\%$  during tests). Stable and reproducible incident electron fluxes of  $1 \text{ nA}\cdot\text{cm}^{-2}$  to  $500 \text{ nA}\cdot\text{cm}^{-2}$  (1, 10, 30, 100, 500  $\text{nA}\cdot\text{cm}^{-2} \pm 3\%$  during tests) with a beam diameter of  $\sim 1 \text{ cm}^2$  FWHM were used [10].

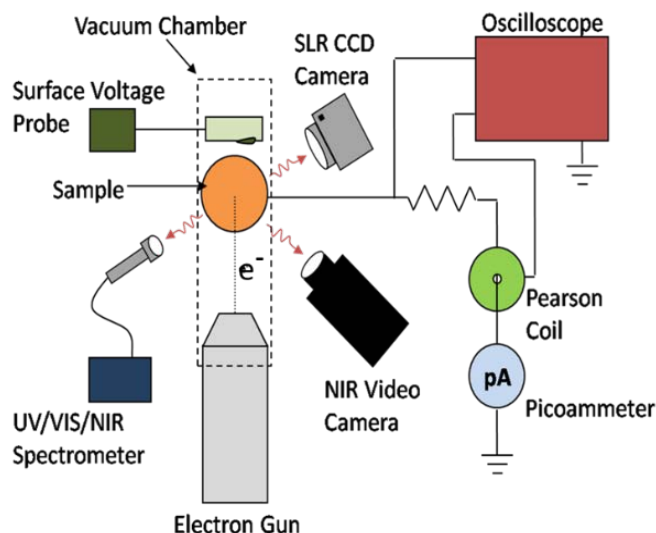


Figure 1 : Diagram of instrumentation used to characterise samples under electron bombardment in EET chamber [11]

The visible/near infrared (Vis/NIR) emission from samples under electron irradiation was measured with two cameras and a spectrometer [9]. Colours and intensity of glow were captured with a single-lens reflex (SLR) CCD camera [Canon, EOS Rebel XT DS126071;  $\sim 400$  nm to  $700$  nm in RGB format, capture time of  $1$  s per frame, with an average spectral response of  $\sim 4 \cdot 10^9$  counts per  $(\text{W}/\text{cm}^2 \cdot \text{sr} \cdot \mu\text{m})$ ]. The low intensity of light was monitored with a Vis/NIR image-intensified video camera [Xybyon, ISG-780-U-3;  $\sim 400$  nm to  $900$  nm,  $30$  frames per s, with an average spectral response of  $\sim 4 \cdot 10^{10}$  counts per  $(\text{W}/\text{cm}^2 \cdot \text{sr} \cdot \mu\text{m})$ ]. The absolute sensitivity of the cameras were calibrated against National Institute of Standards and Technology (NIST) traceable sources. A UV/Vis fibre optic spectrometer (Stellarnet, 13LK-C-SR;  $\sim 350$  nm to  $1080$  nm with  $\leq 0.5$  nm or  $\leq 2$  meV resolution) was used to measure the luminescence emission spectra [1].

The materials studied are industrial samples ( $\sim 1 \times 1 \times 10$  mm) of pyrolytic hexagonal boron nitride (BN), alumina-coated boron nitride (BN/ $\text{Al}_2\text{O}_3$ ), and annealed alumina-coated boron nitride (an-BN/ $\text{Al}_2\text{O}_3$ ). Commercial BN was coated with alumina ( $\sim 0.3$   $\mu\text{m}$  thickness) using an industrial PVD-RF method. The industrial thermal annealing treatment was carried out under vacuum. Surface roughness was equal to  $\sim 0.5$   $\mu\text{m}$  prior to coating [12]. Before irradiation tests, samples were cleaned with methanol and underwent a  $48$  hr vacuum bakeout at  $\sim 375$  K and  $< 1.10^{-3}$  Pa in order to eliminate adsorbed water and volatile contaminants. Subsequently, they were installed in EET chamber at low pressure ( $< 1.10^{-6}$  Pa) for a duration higher than  $30$  hours to allow outgassing prior to irradiation tests. Samples for room temperature tests were mounted on grounded Cu sample holders on the EET sample carousel. Several samples of an-BN/ $\text{Al}_2\text{O}_3$  were mounted side-by-side on a similar grounded Cu sample holder attached to the cryostat in order to increase the exposed sample surface area for temperature-dependent tests.

Accurate prediction of luminescence intensity from multi-layered materials is difficult, especially for materials with different densities, thicknesses, atomic weights, backscatter coefficients and scattering cross-sections [13]. Production of cathodoluminescence results from the deposition of incident electron energy and creation of electron-hole pairs in the material. The energy and depth dependence can be modelled through complex Monte Carlo simulations such as CASINO [14], or can be characterized by a single parameter such as the electron penetration depth or the range [15] in the continuous slow down approximation (CSDA) [16,17]. Table 1 compares values of the penetration depth (depth at peak energy loss) from CASINO simulations to range in the CSDA for bulk  $\text{Al}_2\text{O}_3$  and BN

over the experimental energies. These two measures for energy deposition are consistent with one another, based on a relation developed by Bentabet [18,19]. In a spherical geometric model for a semi-infinite target, Bentabet shows the mean penetration depth  $Z_{12} = (R/2)(1 - \eta)(1 - \frac{\sigma_{Tr}}{\sigma_{el}})$ . The term with the backscatter coefficient  $\eta$  corrects for backscattered electrons and the term involving the transport cross-section  $\sigma_{Tr}$  and the elastic cross-section  $\sigma_{el}$  corrects for inclusion of elastic scatter; both terms are weakly energy dependent with  $(1 - \eta)$  increasing with increasing energy and  $(1 - \frac{\sigma_{Tr}}{\sigma_{el}})$  decreasing such that  $Z_{12} \approx 0.45 \cdot R$  for both materials over the experimental energy range. The CASINO results for h-BN are in fair agreement with limited experimental data [20]. The asymptotic limits of  $\eta$  at high energies were measured for bulk microcrystalline  $\text{Al}_2\text{O}_3$  and h-BN to be 0.2 and 0.15, respectively.

A simple model for luminescence production in the  $\text{Al}_2\text{O}_3$  coating and BN substrate appropriate for the course data presented here follows from a calculation of the electron range (CSDA),  $R(E_{inc})$ , as a function of incident energy,  $E_{inc}$  (Figure 2a) assuming bulk densities  $\rho_m$  of  $3.45 \text{ g.cm}^{-3}$  for BN and  $3.97 \text{ g.cm}^{-3}$  for  $\text{Al}_2\text{O}_3$  [16]. The range of hexagonal  $\text{sp}^2$ -coordinated BN has been approximated using an estimated effective number of valence electrons  $N_V^{eff} = 2.742$ .  $N_V^{eff}$  is predicted from a simple formula—involving band gap energy ( $\sim 6 \text{ eV}$  for hexagonal BN [20], [21]) plus the average atomic weight and atomic number—which was determined by fitting NIST range data in the CSDA [17] and NIST inelastic mean free path data [22] for a wide range of materials [23]. Figure 2(a) also shows the energy-dependent dose rate  $\dot{D}(E_{inc}) = (J_{inc} E_{inc}) / [q_e R(E_{inc}) \rho_m]$  for a  $500 \text{ nA.cm}^{-2}$  non-penetrating beam in the CSDA [8]. Figure 2(b) shows the mean power density deposited by a beam of area  $A$  and range  $R(E_{inc})$ —which is given as  $P(E)/A = (J_{inc} E_{inc}) / q_e$ —in the  $\sim 300 \text{ nm}$  thick alumina coating and the underlying BN substrate of BN/ $\text{Al}_2\text{O}_3$  and an-BN/ $\text{Al}_2\text{O}_3$  samples for a  $500 \text{ nA.cm}^{-2}$  beam. Note that at the lowest incident energy, the electron beam just penetrates the estimated thickness of the  $\text{Al}_2\text{O}_3$  coating. Since electron range increases with beam energy, the dose imparted to the fully penetrated  $\text{Al}_2\text{O}_3$  coating (or similarly, to a thin surface layer of BN) decreases with increasing incident energy from  $\sim 75\%$  at  $5 \text{ keV}$  to  $\sim 4\%$  at  $30 \text{ keV}$  (Figure 2b). Use of the penetration depth for this analysis would shift the power deposition curve to higher energies by about  $35\%$ ; however, penetration depth and range scale with density, so values in Figure 2 are overestimated for less dense coatings and rough surfaces.

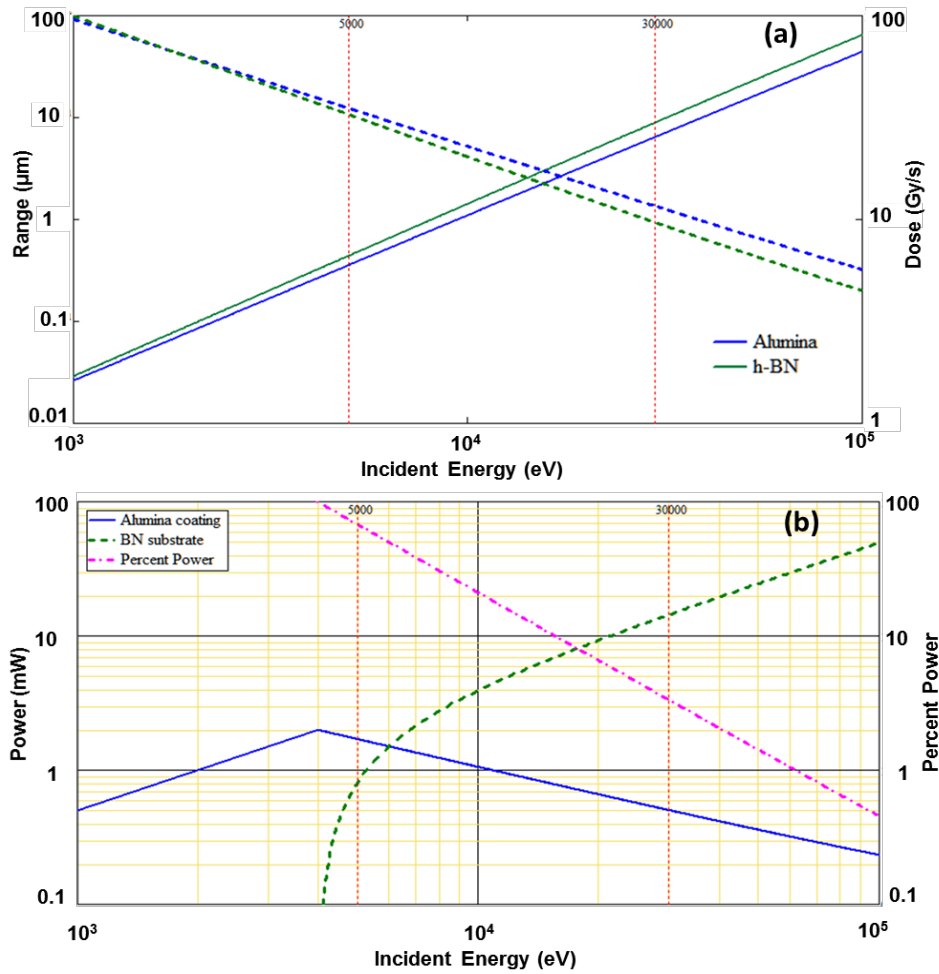


Figure 2 : (a) Range (solid curves, left axis) and dose for non-penetrating beam (dashed curves, right axis) as a function of incident energy. (b) Power deposited (left axis) in 0.3 μm Al<sub>2</sub>O<sub>3</sub> coating (solid curve) and BN substrate (dashed curve) as a function of incident energy for a 500 nA.cm<sup>-2</sup> beam. Percentage of incident electron power absorbed in Al<sub>2</sub>O<sub>3</sub> coating (right axis, dash-dotted curve). The 5 keV to 30 keV energy span of the acquired data is indicated by vertical dashed red lines.

Table. I. Penetration Depth and Range of Al<sub>2</sub>O<sub>3</sub> and h-BN

E (keV)	Bulk Al <sub>2</sub> O <sub>3</sub>			Bulk h-BN		
	Z <sub>12</sub> (μm)	R (μm)	Z <sub>12</sub> /R	Z <sub>12</sub> (μm)	R (μm)	Z <sub>12</sub> /R
5	0.2	0.36	0.56	0.5	0.44	1.1
10	0.7	1.1	0.63	1.1	1.4	0.77
15	1.4	2.1	0.65	1.9	2.8	0.67
20	2.4	3.4	0.71	3.0	4.6	0.66
25	3.6	4.9	0.74	4.3	6.6	0.65
30	5.0	6.5	0.77	5.9	9.0	0.66

## Results and discussion

### a. Results for BN and BN/Al<sub>2</sub>O<sub>3</sub>

Emission spectra as a function of photon energy and wavelength are shown in Figure 3 for an uncoated BN sample irradiated with 5 keV and 30 keV electrons. The red curves represent the emission

spectra raw data; the small intensity of luminescence from BN substrates results in a low signal-to-noise ratio (SNR). These spectra were fitted with least-squares methods for up to four Gaussian peaks with peak central energy, width, and amplitude as fitting parameters. The black curves show the sum of the individual fitted peak profiles and component curves are shown below.

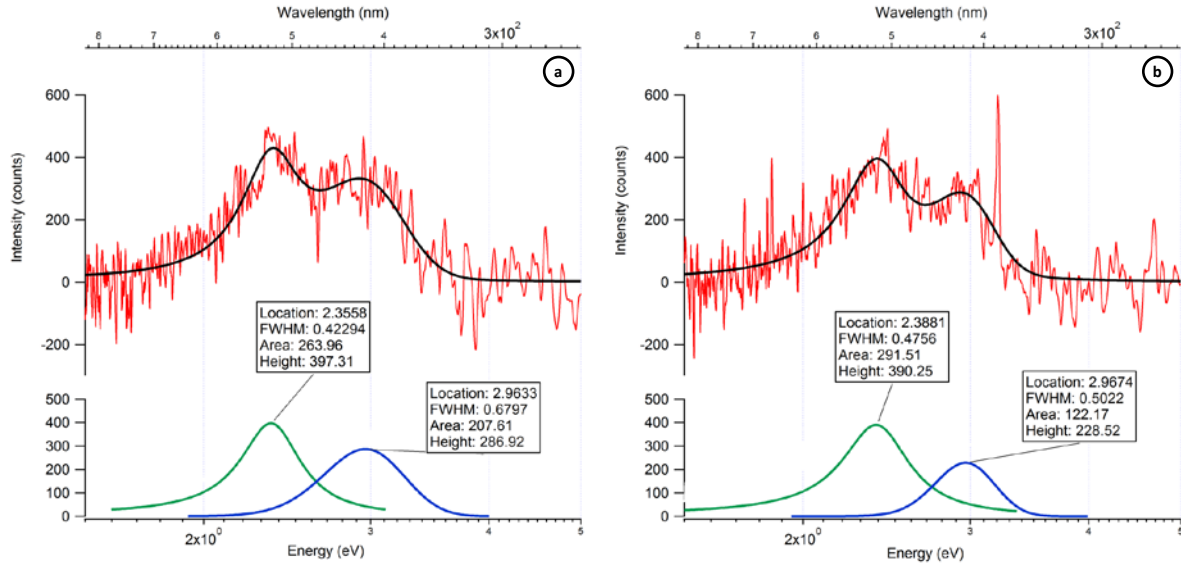


Figure 3 : Emission spectra of BN at room temperature with a 500 nA.cm<sup>-2</sup> incident beam at (a) 5 keV and (b) 30 keV. Lower graphs show the component curves in the fits.

The intensities of BN/Al<sub>2</sub>O<sub>3</sub> spectra have consistently even lower SNR than those of BN. Hence, for clarity sake, the composite fit emission spectra of BN/Al<sub>2</sub>O<sub>3</sub> at various incident electron energies are shown in Figure 4b, while only raw data are shown for BN. Since the observed features were broad, such smoothing is acceptable. Gaussian peak profiles were found to produce better fits than Lorentzian or Voigt functions, as would be expected for long-lived deep level trap states (see below) with very little lifetime broadening [8]. Gaussian widths are a reasonable measure of the DT energy density of states widths, since measured widths are much larger than the  $\lesssim 2$  meV instrumental resolution.

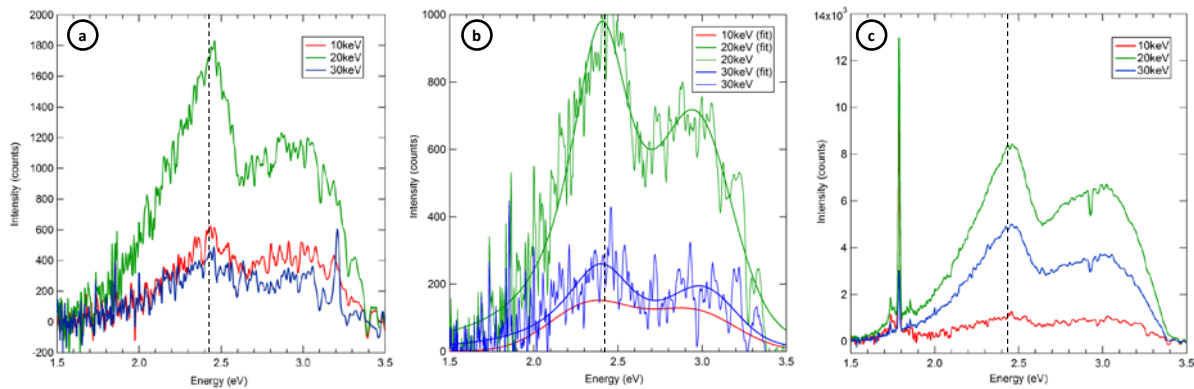


Figure 4 : Emission spectra of (a) BN, (b) BN/Al<sub>2</sub>O<sub>3</sub> and (c) an-BN/Al<sub>2</sub>O<sub>3</sub> acquired at 500 nA.cm<sup>-2</sup> beam current, 10, 20 and 30 keV beam energies, and room temperature

For the BN substrate (Figure 3), two broad peaks were observed at  $\sim 2.4$  eV ( $\sim 516$  nm) and  $\sim 3.0$  eV ( $\sim 416$  nm). Cathodoluminescence spectral features of BN have been difficult to identify and associate with specific defect structures due to the different band gap energies ( $\sim 4.5$  eV to  $\sim 6.5$  eV) [20] and

structures associated with cubic ( $sp^3$ -bonded) c-BN [24], [25], hexagonal ( $sp^2$ -bonded) h-BN [20], [24], [26], boron nitride nanotubes [24], and disordered BN such as pyrolytic pBN [24]. Broad peaks at 2.48 eV (attributed to multivacancy complexes of B and N vacancies in c-BN) and 3.12 eV (of unknown origin) have been reported in CL spectra of higher purity c-BN close to our observed peaks at  $\sim 2.4$  eV and  $\sim 3.0$  eV. However, sharper peaks of similar intensities at 2.81 eV, 3.01 eV and 3.20 eV attributed to c-BN and a broad intense peak at  $\sim 3.55$  eV attributed to h-BN seen in [25] were not observed in our spectra.

The intensities of BN/Al<sub>2</sub>O<sub>3</sub> spectra are lower than those of BN. The integrated peak intensities at given incident energies of both of the two observed broad  $\sim 2.40$  eV (Figure 5a) and  $\sim 2.98$  eV (Figure 5b) peaks for the BN/Al<sub>2</sub>O<sub>3</sub> spectra are consistently  $\sim 50\%$  smaller than corresponding peaks for BN. However, the shapes of the  $\sim 2.40$  eV and  $\sim 2.98$  eV peaks—indeed the shape of the full spectra from 1.5 eV to 4.5 eV—are very similar for the BN and BN/Al<sub>2</sub>O<sub>3</sub> spectra (Figure 4). The peak energies of the two observed broad  $\sim 2.40$  eV and  $\sim 2.98$  eV peaks for BN/Al<sub>2</sub>O<sub>3</sub> spectra coincide with those of the BN spectra to within  $< 0.5\%$  above 10 keV incident energies and deviate at lower energies by  $< 1.5\%$  (Figure 5e); numerical uncertainty due to the fitting process is  $\lesssim 1\%$ . The peak widths for both peaks show little change from the mean high energy peak FWHM of  $0.49 \pm 0.04$  eV over the full incident energy range and are similar for both BN and BN/Al<sub>2</sub>O<sub>3</sub> (Figure 5f). The ratios of intensities of  $\sim 3.0$  eV peak to  $\sim 2.4$  eV peak at the same incident energy ( $I_{2.98}/I_{2.40}$ ) for both BN and BN/Al<sub>2</sub>O<sub>3</sub> has a mean ratio of 0.41 with average deviation of  $< 2\%$  above 10 keV incident energies, though the ratios do increase substantially at lower energies (Figure 5e). The fact that the addition of a coating does not change the broad shape of the spectra and produces no new sharp spectral features—as are seen for an-BN/Al<sub>2</sub>O<sub>3</sub> (see below)—suggests that the as-deposited PVD-RF Al<sub>2</sub>O<sub>3</sub> coating of BN/Al<sub>2</sub>O<sub>3</sub> does not have appreciable cathodoluminescent active or absorptive states in the 1.5 eV to 4.5 eV range. Rather, the Al<sub>2</sub>O<sub>3</sub> coating acts to absorb about half of the power from incident electrons, thereby reducing the dose to BN and the resulting BN emission intensity as the incident beam is attenuated passing through the Al<sub>2</sub>O<sub>3</sub> coating.

Additional information about the power deposition can be deduced from the relative changes in emission intensity as a function of incident electron energy. Given the conclusion above, that the unannealed Al<sub>2</sub>O<sub>3</sub> coating does not contribute appreciably to the emission spectra, these energy dependent changes most likely result from difference in the rough surface layer and bulk of the BN substrate. Such surface state effects could result from the mechanical treatment of the BN surface which produces a local mechanical strain or from the significant surface roughness. There is a surprisingly consistent dependence on incident energy for both the  $\sim 2.98$  eV and  $\sim 2.4$  eV peaks of both BN and BN/Al<sub>2</sub>O<sub>3</sub> samples. Both peaks for both materials show a distinctly different behaviour in relative intensity (Figure 5c and d), peak position (Figure 5e), and (to a lesser extent) peak width (Figure 5f) at lower incident energy electrons below 15 keV [which are more surface sensitive due to reduced electron penetration (see Figure 2b)]. Figure 5c shows the relative change of the integrated intensity of the  $\sim 3.0$  eV and  $\sim 2.4$  eV peaks for both BN and BN/Al<sub>2</sub>O<sub>3</sub> (*i.e.*, the integrated peak intensities normalized to largest intensity for each peak of each sample), plotted as a function of incident energy. The horizontal dashed red line indicates mean low energy behavior at  $< 15$  keV,  $\sim 30\%$  of the maximum normalized intensities for each peak and sample near 20 keV. The sloped dashed red line (in Figure 5c) is a linear fit to decreasing intensity above 15 keV, with a decrease of 76% from 20 keV to 30 keV. A similar decrease of 50% is predicted for the fraction of power deposited in a  $0.3 \mu\text{m}$  surface layer from 20 keV to 30 keV (Figure 2b). Both the BN  $\sim 2.40$  eV and BN  $\sim 2.98$  eV peaks in both the BN and BN/Al<sub>2</sub>O<sub>3</sub> spectra show a  $\sim 40$  meV ( $\sim 1.5\%$ ) shift to lower energies (see Figure 5e) at incident electrons energies  $< 15$  keV. This suggests that at lower incident energies [where a higher fraction of the incident power is deposited in the surface layer], BN surface DT states are more weakly bound than the bulk DT states. Substantial decreases in integrated peak intensities for the  $\sim 2.40$  eV and  $\sim 2.98$  eV in both BN and BN/Al<sub>2</sub>O<sub>3</sub> spectra are likewise observed at lower incident energies (Figure 5 a and b). Further, the

relative density of deeper traps to shallower traps—as reflected in the ratio of peak intensities ( $I_{2.98}/I_{2.40}$ ) (Figure 5d)—increases below 15 keV for both BN and BN/ $Al_2O_3$  samples, with BN/ $Al_2O_3$  exhibiting a larger change than BN; this could indicate that the relative fraction of surface states is larger for BN/ $Al_2O_3$  than for BN samples and for the  $\sim 2.98$  eV defect than for the  $\sim 2.40$  eV defect.

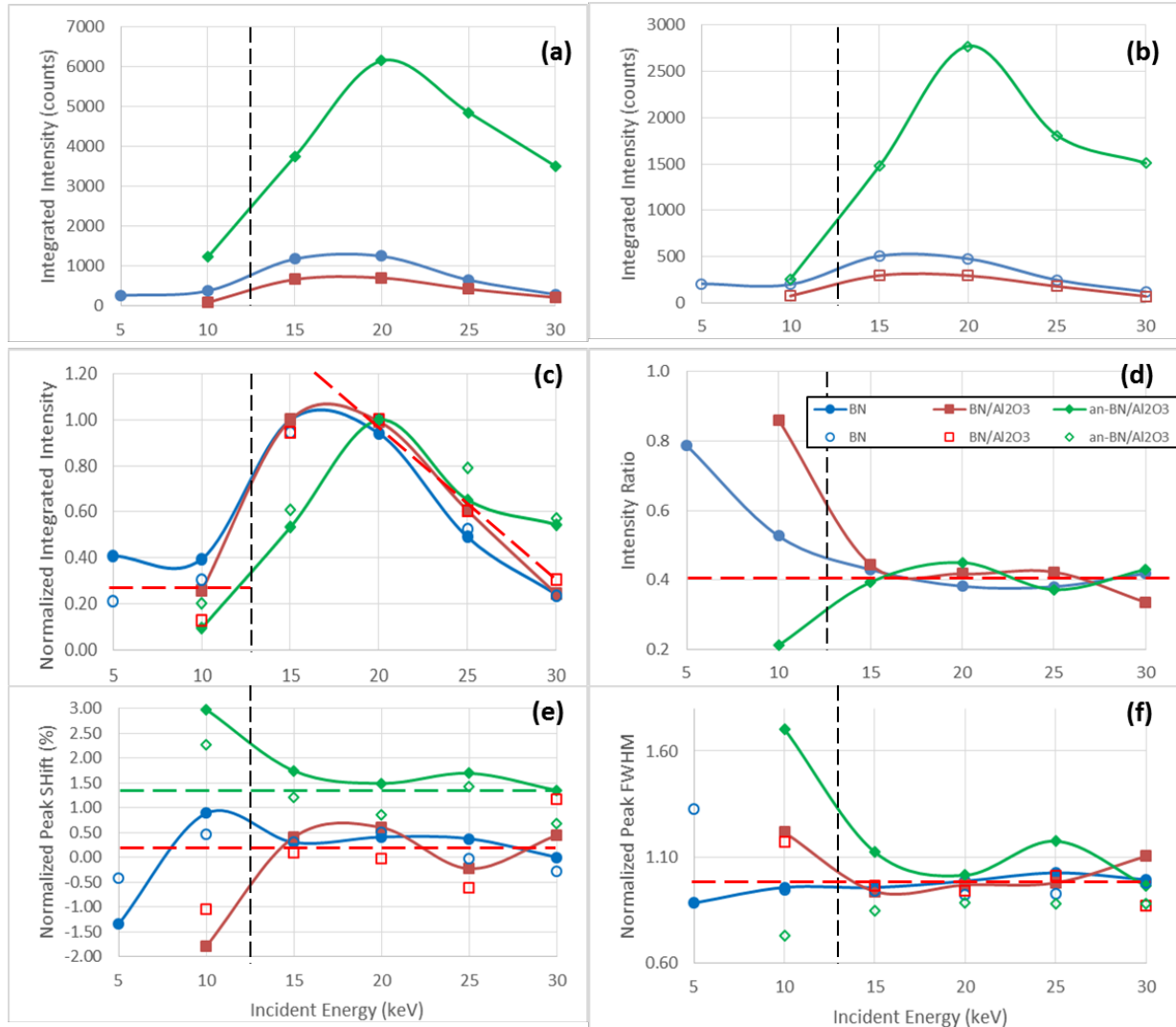


Figure 5 : BN cathodoluminescence peak fitting parameters as a function of incident electron energy for  $\sim 2.4$  eV (filled) and  $\sim 2.98$  eV (open) peaks at  $500 \text{ nA.cm}^{-2}$  beam current for the three samples BN (circle), BN/ $Al_2O_3$  (square) and an-BN/ $Al_2O_3$  (triangle). Vertical dashed black lines indicate the boundary between low energy peak behavior and high energy peak behavior between 10 keV and 15 keV. (a and b) Integrated peak intensities, for  $\sim 2.4$  eV and  $\sim 2.98$  eV peaks, respectively. (c) Integrated peak intensities normalized to largest intensity for each peak of each sample. The horizontal dashed red line indicates mean low energy behavior. The sloped dashed red line is a linear fit to decreasing intensity above 15 keV, with a slope of  $-76\%$  per 10 keV. (d) Ratio of intensities of  $\sim 2.98$  eV peak to  $\sim 2.4$  eV peak ( $I_{2.98}/I_{2.40}$ ), with 0.41 mean ratio at high energies (horizontal dashed red line). (e) Percent shift in peak energy normalized to the mean low energy unannealed peak positions at  $2.388 \pm 0.005$  eV (solid) and  $2.995 \pm 0.005$  eV (open), respectively. The an-BN/ $Al_2O_3$  (triangle) peaks have a mean 1.3% shift at high energies. (f) Peak width (FWHM) normalized to the mean high energy peak width of  $0.49 \pm 0.04$  eV

### **b. Results for an-BN/Al<sub>2</sub>O<sub>3</sub>**

Emission spectra of an-BN/Al<sub>2</sub>O<sub>3</sub> for several incident electron energies are dramatically different than BN and BN/Al<sub>2</sub>O<sub>3</sub> spectra. Overall, CL intensity from an-BN/Al<sub>2</sub>O<sub>3</sub> is substantially higher, with higher SNR; consequently, the curves shown in Figure 4c are raw data rather than fitted curves.

First, we consider the broad peaks at ~2.40 eV and ~2.98 eV which we previously attributed to the BN substrate. The CL intensities of these two peaks at 20 keV when the peak intensity is highest are ~4-6 times more intense than the corresponding BN peaks and 8-12 times more intense than those of unannealed BN/Al<sub>2</sub>O<sub>3</sub> (Figure 4a and b). The increase in an-BN/Al<sub>2</sub>O<sub>3</sub> integrated peak intensities is only about twice that of BN at 10 keV, but increases with increasing incident energies to about 10 times at 30 keV (Figure 5 a and b). These increased enhancements for more penetrating higher energies suggest that they originate preferentially from deeper BN material. It was suggested in a companion study—which included measurements of Raman spectroscopy, XPS, electrical conductivity, and electron-induced surface charging and relaxation—that the annealing treatment of an-BN/Al<sub>2</sub>O<sub>3</sub> generated a higher density of physical and chemical defects especially near the surface [27]. Thermal annealing could allow either chemical or physical defects inherent in the surface layers to diffuse further into the bulk. An alternate cause of the observed increased emissions from BN could be due to reduced surface charging from the incident electron beam. The reduced charging could result from increased total electron emission [28], as well as from increased conductivity which increased charge dissipation. Measurements showed the bulk conductivity of an-BN/Al<sub>2</sub>O<sub>3</sub> was 15 times that of BN and 40 times that of unannealed BN/Al<sub>2</sub>O<sub>3</sub> [27]. Negative surface potential of up to 3500 V was measured for BN irradiated with a 11 keV beam; this was reduced to ~1700 V for BN/Al<sub>2</sub>O<sub>3</sub> and ~200 V for an-BN/Al<sub>2</sub>O<sub>3</sub> [27]. Enhanced negative surface charging reduces the landing energies of incident electrons, thereby reducing the absorbed power and the penetration range and hence reducing the CL intensity [7].

There are some small differences in the shape of these broad peaks at ~2.40 eV and ~2.98 eV. The ~2.40 eV and ~2.98 eV peak energies of an-BN/Al<sub>2</sub>O<sub>3</sub> at incident energies >10 keV are about 1.5% higher than those for BN and BN/Al<sub>2</sub>O<sub>3</sub> spectra and increase modestly at lower energies instead of decreasing as for BN and BN/Al<sub>2</sub>O<sub>3</sub> peaks (Figure 5d). The widths of these two peaks are similar for all three materials, with some differences below 15 keV (Figure 5f). The relative density of deeper traps to shallower traps—as reflected in the ratio of peak intensities ( $I_{2.98}/I_{2.40}$ ) (Figure 5d)—are nearly identical for all three samples above 10 keV, although the ratio does decrease for an-BN/Al<sub>2</sub>O<sub>3</sub> below 15 keV. The energy dependences of the normalized integrated intensities exhibit very similar energy dependencies for all three materials (Figure 5c). Altogether, these differences in spectral shape suggest the added intensity in the broad an-BN/Al<sub>2</sub>O<sub>3</sub> spectra is not from the Al<sub>2</sub>O<sub>3</sub> coating, though we cannot rule out some contributions due to broad CL peaks in similar energy ranges of 3.5 eV to 5.0 eV sometimes observed for Al<sub>2</sub>O<sub>3</sub> materials [29], [30].

Second, we consider additional sharp features in Figure 4c. These include a strong sharp emission peak at ~1.785 eV with numerous small sharp satellite peaks visible in Figure 6, plus a sharp absorption peak at ~2.93 eV. Annealing induces both chemical and structural changes in the Al<sub>2</sub>O<sub>3</sub>, leading to CL which can be clearly attributed to the annealed Al<sub>2</sub>O<sub>3</sub> surface layer. Chemical characterization of an-BN/Al<sub>2</sub>O<sub>3</sub> with Raman [27] and XPS [12] methods found evidence for (Cr<sup>3+</sup>) impurities and chemical bonds of compounds Al(2p) and O(1s). O vacancies are known to be produced in Al<sub>2</sub>O<sub>3</sub> in a reducing (vacuum) environment [30] and by electron irradiation [31]; these have been associated with luminescence attributed to one electron (F<sup>+</sup> emission) or two electron (F emission) trapping processes [30].

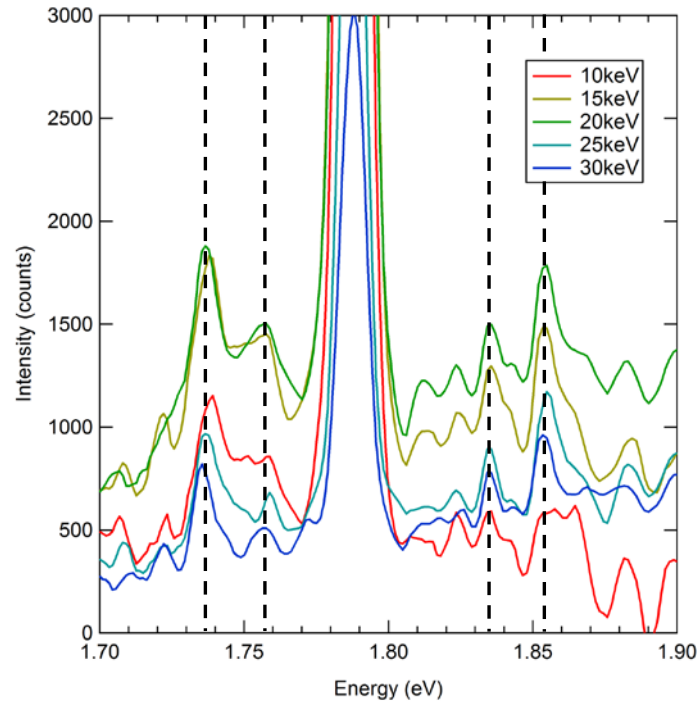


Figure 6 : Emission spectra of an-BN/Al<sub>2</sub>O<sub>3</sub> near the 1.785 eV ruby peak acquired at 500 nA.cm<sup>-2</sup> beam current, 10,15, 20, 25 and 30 keV beam energies, and room temperature. Larger satellite peaks are observed at ~1.737 eV, ~1.758 eV, ~1.835 eV and ~1.853 eV are indicated by vertical dashed lines.

The most prominent feature attributed to the alumina layer in Figure 4c is a sharp and intense low energy peak at ~1.785 eV. This peak is called the “ruby peak” because it is characteristic of ruby [crystalline Al<sub>2</sub>O<sub>3</sub> (sapphire) of the mineral family of corundum with Cr impurities]. This peak corresponds to the no-phonon line caused by localized chemical defects (colour centres) related to Cr<sup>3+</sup> impurities [4], [27], [30], [32], [33]. Very low concentrations of <5 ppm of Cr<sup>3+</sup> can cause intense emissions [34].

Around this intense no-phonon peak at ~1.785 eV, symmetric peaks were observed at ~1.758 eV and ~1.835 eV (Figure 6) corresponding to vibrational (phonon-) assisted electron transitions, similar to those seen in previous studies [4], [27], [32]. Indeed six or more smaller satellite peaks are evident in Figure 6, evenly spaced at 14±1 meV intervals, at energies both above and below the 1.785 eV peak. This incremental energy is the phonon energy. Additional satellite peaks are observed at ~1.737 eV and 1.853 eV; peaks at these energies have been previously attributed to point defects of Fe<sup>2+</sup> and Ti<sup>4+</sup> in Al<sub>2</sub>O<sub>3</sub> [30].

A narrow absorption peak is observed at ~2.93 eV, superimposed on the emission from the ~2.98 eV BN peak. Charge carriers are excited from deep traps (DT) to shallow traps (ST) in the annealed alumina coating by absorption of photons coming from the luminescence of BN substrate. Carriers excited to these ST states can then be thermally excited into conducting states, thereby activating charge transport in the Al<sub>2</sub>O<sub>3</sub> layer. This absorption band is near a band observed at ~2.89 eV from radiation induced defects [35].

All these chemical defects generating low energy electron transitions are activated by thermal annealing of the alumina coating. Consequently, the annealing process must generate several kinds of relatively low energy localized defects with substantial densities within the Al<sub>2</sub>O<sub>3</sub> band gap. These low energy trap states can potentially act to increase conductivity in the alumina layer in several ways. Absorption of higher energy photons from the BN luminescence could excite electrons from the low energy Al<sub>2</sub>O<sub>3</sub> chemical defect states directly into the CB or into ST states which are then thermally

excited into the CB. Further, more mobile charge carriers in the annealed sample would reach recombination centres more easily thereby enhancing electron-hole recombination. This in turn may act to limit charging in the annealed alumina layer as compared to the unannealed alumina layer or the BN surface layer, thereby increasing the incident electrons flux reaching the BN and enhancing BN CL intensities in the an-BN/Al<sub>2</sub>O<sub>3</sub> samples.

The glow intensity of an-BN/Al<sub>2</sub>O<sub>3</sub> after the end of irradiation is shown in Figure 7. During this relaxation phase after the beam is turned off, delayed luminescence (phosphorescence) is observed with an exponential decrease in intensity with two discernible decay constants of  $0.81 \pm 0.01$  s and  $5.4 \pm 0.1$  s. This delayed luminescence is characteristic of recombination processes of charges carriers after irradiation that involves detrapping of longer-lifetime trap states at the beginning of the relaxation phase.

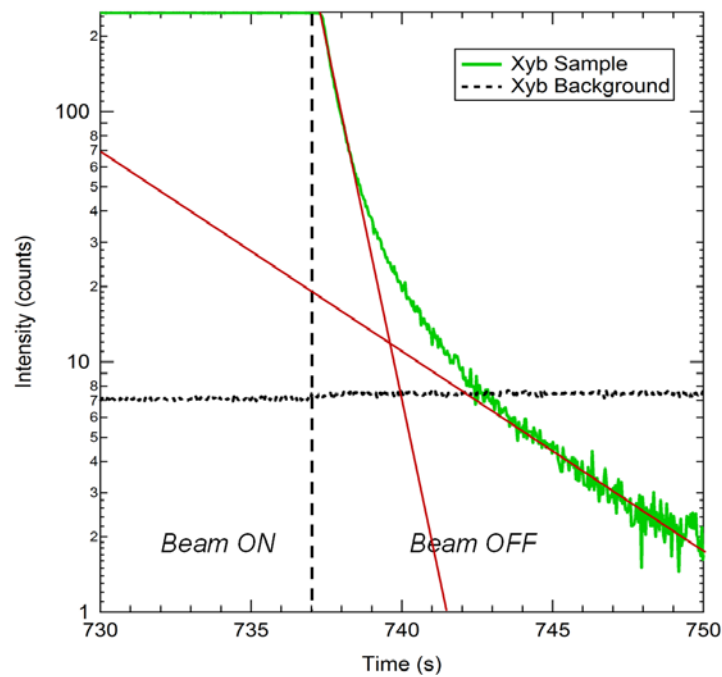


Figure 7: Delayed luminescence of an-BN/Al<sub>2</sub>O<sub>3</sub>. The electron beam (30 keV at 500 nA.cm<sup>-2</sup>) incident on a room temperature sample is turned off at 737 s, as denoted by the vertical dashed line. The CL intensity measured with the Xybion CCD camera (green solid line) has had the background (black curve) subtracted; the camera is saturated when the beam is on. Red lines are exponential decay fits with decay constants of  $0.81 \pm 0.01$  s and  $5.4 \pm 0.1$  s.

### c. Influence of temperature

A thorough study of an-BN/Al<sub>2</sub>O<sub>3</sub> at various temperatures was performed in order to get more information about electron transitions within the band gap of the annealed coating. Figure 8 shows the temperature evolution of the strong CL “ruby” peak (related to Cr<sup>3+</sup> defects) from an-BN/Al<sub>2</sub>O<sub>3</sub> exposed to an electron beam with energy of 5 keV and flux of 500 nA.cm<sup>-2</sup>. This low incident energy was chosen for three main reasons: (i) at this energy with a electron penetration range is  $\sim 0.25$   $\mu$ m (Figure 2a), most electrons were deposited in the  $\sim 0.3$   $\mu$ m thick alumina coating, thereby optimising the CL intensity from the annealed Al<sub>2</sub>O<sub>3</sub> layer; (ii) to limit charging of the ceramic sample, thereby avoiding a decrease in the local incident energy which would affect CL measurements as a function of time and (iii) lower incident energies above the second crossover energies such as 5 keV have total electron yields near unity that cause less charging.

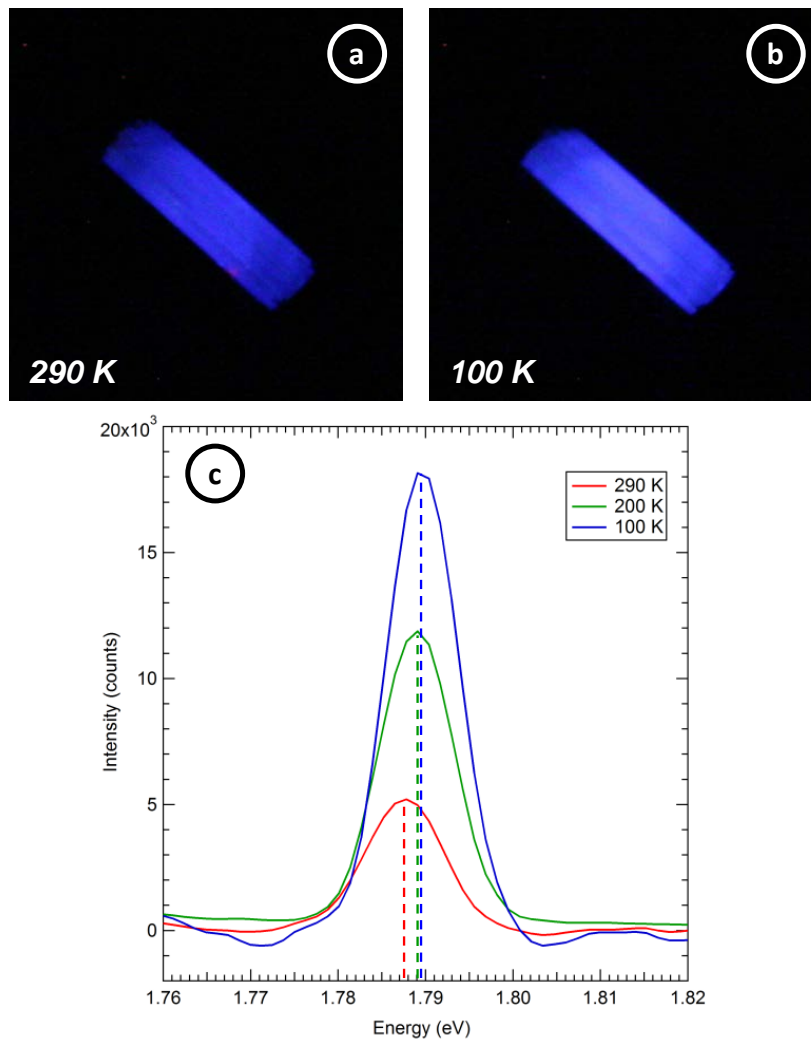


Figure 8 : Evolution of cathodoluminescence of an-BN/Al<sub>2</sub>O<sub>3</sub> as a function of temperature under electron bombardment at 5 keV and 500 nA.cm<sup>-2</sup>. (a-b) Intensity evolution captured through SLR CCD camera photographs. (c) Temperature variation of “ruby” peak at ~1.785 eV.

The overall CL intensity increases when the temperature decreases and the luminescence hue is more magenta than violet especially at the center of specimen (Figure 8). That is due to a larger increase of the “ruby” peak intensity than that of the higher energy broad peaks attributed to the BN substrate.. Powell [32], [36] and Green [33] performed detailed studies of the temperature dependence of the “ruby” peak (~1.785 eV). Green showed that the conversion efficiency (which is directly proportional to CL intensity) is linearly proportional to the optical phonon density which increases exponentially at lower temperatures as an Arrhenius function; his theoretical prediction of a ~20 increase in CL intensity from room temperature to 100 K is larger than the four-fold increase shown in Figure 8c.

This increase in the intensity of “ruby” peak is due to a relative increase of electron transitions to the more shallow (low energy) DT states (emission from Cr<sup>3+</sup>-center : transition  ${}^2E \rightarrow {}^4A_2$  [37]). Indeed, when T decreases the deeper traps (blue and violet BN traps) become more filled because charges are decreasingly thermally excited into ST or CB states, limiting the number of these traps that electrons can decay into and emit photons. By contrast, the occupied density of the shallower DT traps (red an-BN/Al<sub>2</sub>O<sub>3</sub> traps) remains lower due to thermal excitations into the ST and CB and thus electron transitions from ST into the red traps and the accompanying CL remain high. The same sort of increase in CL with decreasing temperature was observed for four DT states in SiO<sub>2</sub>. The behavior of these SiO<sub>2</sub> peaks was attributed to the thermal dependence of the occupancy of the deep traps, as explained by a

model for CL for highly disordered insulating materials based on band models of the localized disordered trap states found in the forbidden band gap region of insulating materials. CL intensity increases with decreasing occupancy and increased number of available low energy states to decay into [8], [29].

Figure 8c shows a small ( $\sim 22$  meV from 100 K to 290 K) red shift of the “ruby” peak at higher temperatures. This red shift of the “ruby” peak was similar to small decreases in peak energy observed for three of the four SiO<sub>2</sub> peaks; the peak shifts can be explained as due to energy of the emitted photons increasing as the mean occupation level of the DT decreases; this too is related to the occupancy of the DT states [29].

#### d. Influence of long irradiation time (dose)

An annealed coated sample was irradiated for several hours under high electron flux in order to study the evolution of defects and their occupation in an-BN/Al<sub>2</sub>O<sub>3</sub> as a function of the ionizing dose. For the same reasons noted in Section c., an incident energy of 5 keV was used to irradiate the sample.

Figure 9a shows the temporal evolution of CL intensity under prolonged irradiation, with a noticeable diminution in the red colour of the sample at lower temperatures. The general intensity, brightness and hue of CL of the an-BN/Al<sub>2</sub>O<sub>3</sub> sample approach those of the BN substrate over irradiation time. However, some regions of the an-BN/Al<sub>2</sub>O<sub>3</sub> sample becomes brown (dark spots on the picture in Figure 9a for 1177 min exposure). On occasion, the sample would abruptly increase in intensity after prolonged beam exposure; this and the asymptotic behaviour suggest that the intensity variations were related to sample charging and a concomitant decrease in power deposited in the sample. This is consistent with the temporal evolution of the surface potential of an-BN/Al<sub>2</sub>O<sub>3</sub>, which after 300 min exposed to a 750 nA.cm<sup>-2</sup> 20 keV beam at room temperature reached approximately -3700 V [12], [27].

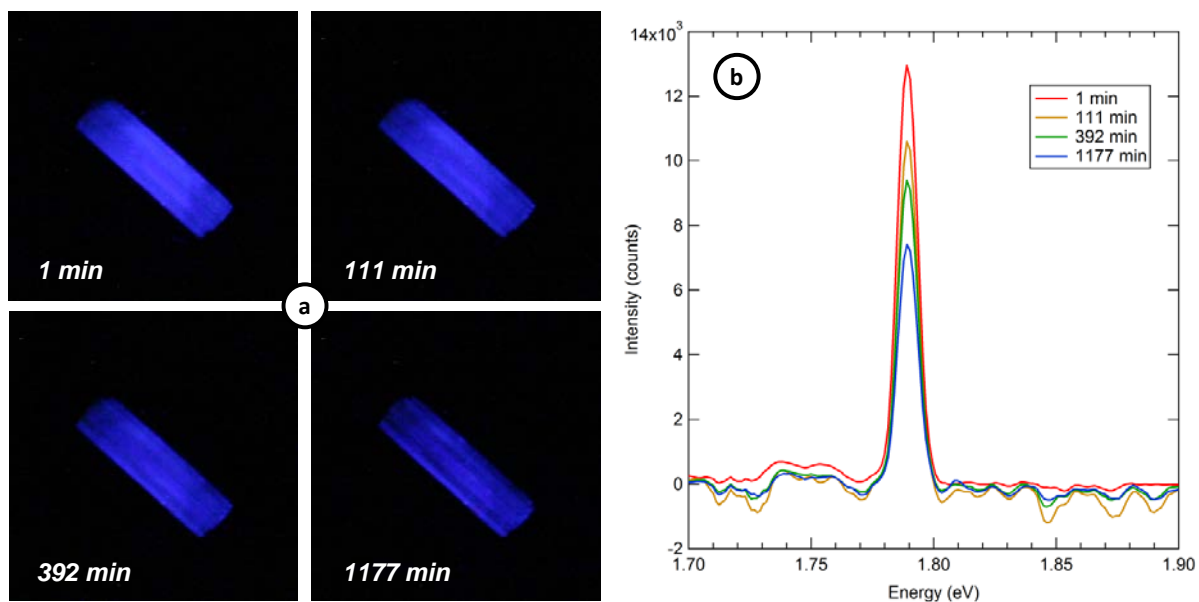


Figure 9 : Evolution of cathodoluminescence of an-BN/Al<sub>2</sub>O<sub>3</sub> as a function of irradiation time under electron bombardment of 5 keV at 500 nA.cm<sup>-2</sup> and at 110 K: (a) Evolution of overall intensity captured through SLR CCD camera photographs. (b) Emission CL spectra of “ruby” peak at  $\sim 1.79$  eV.

More specifically, the CL intensity of the an-Al<sub>2</sub>O<sub>3</sub> “ruby” peak decreases  $\sim 50\%$  after 1177 min (Figure 9b). This decrease could be a result of the surface potential build up described above.

Alternately, the decrease could result from CL saturation as the occupancy of final “ruby” trap increases with charge accumulation thereby diminishing the CL transition rate [29]. The CL decrease could also result from chemical or structural evolution of the Al<sub>2</sub>O<sub>3</sub> surface from defect modification, contamination or aging [12]. Further details—related to CL—of the effects of electron irradiation on the electrical aging from an-BN/Al<sub>2</sub>O<sub>3</sub> samples are discussed in [12], [27].

## Conclusion

A thorough investigation of defects states in samples of boron nitride (BN), alumina coated BN (BN/Al<sub>2</sub>O<sub>3</sub>), and annealed BN with Al<sub>2</sub>O<sub>3</sub> coating (an-BN/Al<sub>2</sub>O<sub>3</sub>) was carried out under electron bombardment through cathodoluminescence (CL) measurements. The natures and densities of defects and their occupation were studied as a function of incident electron energy and flux, sample temperature, and dose. Evidence suggests that much of the broad signature emission attributed to BN was produced in the rough near surface regions of the samples and its CL intensity was diminished by surface charging. The Al<sub>2</sub>O<sub>3</sub> coating deposited through physical vapour deposition does not have substantial CL-active defects, which could impact the surface conductivity of Al<sub>2</sub>O<sub>3</sub> coating. However, the vacuum thermal annealing treatment performed on BN/Al<sub>2</sub>O<sub>3</sub> has a very significant effect on CL emissions. Indeed, this thermal treatment generates many sharp features in the CL spectra ascribed to specific types of defects in the sample and especially in the Al<sub>2</sub>O<sub>3</sub> coating. This increase of the nature and density of Al<sub>2</sub>O<sub>3</sub> defects states, especially Cr<sup>3+</sup> defects, seems to favour electron transitions and charge mobility under electron irradiation. The influence of temperature on electron transitions from the conduction band (CB) and shallow trap (ST) states to red trap levels (upper band of DT) is significant. In fact, these states become predominant when the temperature decreases and charges in the deeper bands remain trapped. Nonetheless, the CL decreases as a function of time under high electron flux. The ionizing dose deposited in the Al<sub>2</sub>O<sub>3</sub> coating gradually degrades this material which affects electron transitions.

## Acknowledgement

Authors would like to thank A. Jensen and A. Souvall of Materials Physics Group for their technical support. The authors gratefully acknowledge the laboratories and companies which contributed to this international collaboration, including the USU Physics Department, ONERA Toulouse, CIRIMAT and THALES.

## References

- [1] A. Evans Jensen et al., « Properties of cathodoluminescence for cryogenic applications of SiO<sub>2</sub>-based space observatory optics and coatings », *Proc. Soc. Photo-Optical Instrum. Engineers Cryogenic Optical Systems and Instruments Conf.*, vol. **8863**, p. 88630A1-88630A10, 2013.
- [2] U. Helmersson, M. Lattemann, J. Bohlmark, A. P. Ehiasarian, and J. T. Gudmundsson, « Ionized physical vapor deposition (IPVD): A review of technology and applications », *Thin Solid Films*, vol. **513**, no 1-2, p. 1-24, 2006.
- [3] B. V. Prokofiev, « Pyrolytical Boron Nitride as a Window Material for High Power Microwave Electron Devices », *8th International of Vacuum Electron Sources Conference and Nanocarbon (IVESC)*, IEEE Publ., Piscataway, NJ, p. 205-206, 2010.
- [4] M. J. Treadaway, B. C. Passenheim, and B. D. Kitterer, « Luminescence and Absorption of Electron-Irradiated Common Optical Glasses, Sapphire, and Quartz », *IEEE Trans. Nucl. Sci.*, vol. **22**, no 6, p. 2253-2258, 1975.
- [5] R. Haubner, M. Wilhelm, R. Weissenbacher, and B. Lux, « Boron nitrides—properties, synthesis and applications », *High Perform. Non-Oxide Ceram. II*, vol. **102**, Structure and Bonding, Springer-Verlag, Berlin, p. 1-45, 2002.

- [6] J. F. Fowler, « Radiation-induced Conductivity in the Solid State, and Some Applications », *Phys. Med. Biol.*, **vol. 3**, no 4, p. 395-410, 1959.
- [7] J. R. Dennison, « Characterization of Electrical Materials Properties Related to Spacecraft Charging », Radiation Capabilities for the Europa Jupiter System Missions Instrument Workshop, Johns Hopkins Applied Physics Laboratory, Laurel, MD, 2009.
- [8] A. Jensen, « Modeling the Defect Density of States of Disordered SiO<sub>2</sub> Through Cathodoluminescence », Master Thesis, USU, 2014.
- [9] J. Dekany, R. H. Johnson, G. Wilson, A. Evans, and J. R. Dennison, « Ultrahigh Vacuum Cryostat System for Extended Low-Temperature Space Environment Testing », *IEEE Trans. Plasma Sci.*, **vol. 42**, no 1, p. 266-271, 2014.
- [10] G. Wilson, J. R. Dennison, A. E. Jensen, and J. Dekany, « Electron Energy-Dependent Charging Effects of Multilayered Dielectric Materials », *IEEE Trans. Plasma Sci.*, **vol. 41**, no 12, p. 3536-3544, 2013.
- [11] A. Evans, J. R. Dennison, G. Wilson, and J. Dekany, « Low-Temperature Cathodoluminescence in Disordered SiO<sub>2</sub> », *IEEE Trans. Plasma Sci.*, **vol. 42**, no 1, p. 272-277, 2014.
- [12] K. Guerch, « Etude des propriétés physiques et électriques de matériaux céramiques utilisés en application spatiale », PhD Thesis, Université Toulouse III - Paul Sabatier, 2015.
- [13] L J Brillson « Applications of depth-resolved cathodoluminescence spectroscopy,» *J. Phys. D: Appl. Phys.* **45**, p. 183001, 2012.
- [14] P. Hovington, D. Drouin and R. Gauvin « » *Scanning* **19**, p. 1–14, 1997. Casino 3.3 code is available at <http://www.gel.usherbrooke.ca/casino/>
- [15] L. Reimer, *Scanning Electron Microscopy: Physics of Image Formation and Microanalysis*, 2nd Ed., Springer-Verlag, Heidelberg. 1998.
- [16] G. Wilson and J. R. Dennison, « Approximation of Range in Materials as a Function of Incident Electron Energy », *IEEE Trans. Plasma Sci.*, **vol. 40**, no 2, p. 291-297, 2012.
- [17] National Institute of Standards and Technology, 2010, "ESTAR, Stopping Power and Range Tables for Electrons," (<http://physics.nist.gov/PhysRefData/Star/Text/ESTAR.html>).
- [18] A. Bentabet, « Spherical geometric model for absorption electrons/positrons phenomenon: Application to the mean penetration depth calculation », *Vacuum*, **vol. 86**, p. 1855-1859, 2012,
- [19] A. Bentabet, « Range and Stopping Power Energy Relationships for 0.5–30 Kev Electron Beams Slowing Down in Solids: Analytical Model, » *Modern Physics Letters B*, **vol. 28**, No. 1, p. 1450006, 2014.
- [20] M. Silly et al., « Luminescence properties of hexagonal boron nitride: Cathodoluminescence and photoluminescence spectroscopy measurements », *Phys. Rev. B*, **vol. 75**, n° 8, 2007.
- [21] Y. Kubota, K. Watanabe, O. Tsuda, and T. Taniguchi, « Deep Ultraviolet Light-Emitting Hexagonal Boron Nitride Synthesized at Atmospheric Pressure », *Science*, **vol. 317**, no 5840, p. 932-934, 2007.
- [22] National Institute of Standards and Technology, 2010, "NIST Electron Inelastic-Mean-Free-Path Database: Version 1.1," (<http://www.nist.gov/data/nist71.htm>).
- [23] G. Wilson, A. Starley, L. Phillipps and JR Dennison, "Predictive Formula for Electron Penetration Depth of Diverse Materials over Large Energy Ranges," *submitted to IEEE Tran. Plasma Science*, 6 pp., 2017.
- [24] B. Berzina et al., « Photoluminescence excitation spectroscopy in boron nitride nanotubes compared to microcrystalline h-BN and c-BN », *Phys. Status Solidi C*, **vol. 2**, no 1, p. 318-321, 2005.
- [25] W. J. Zhang, H. Kanda, and S. Matsumoto, « Cathodoluminescence of cubic boron nitride films deposited by chemical vapor deposition », *Appl. Phys. Lett.*, **vol. 81**, no 18, p. 3356-3358, 2002.
- [26] M.-S. Jin and N.-O. Kim, « Photoluminescence of Hexagonal Boron Nitride (h-BN) Film », *J. Electr. Eng. Technol.*, **vol. 5**, no 4, p. 637-639, 2010.
- [27] K. Guerch, T. Paulmier, J. R. Dennison, J. Dekany, P. Lenormand, and S. Guillemet-Fritsch, « Electrical Properties of Annealed and Coated Boron Nitride Under Electron-Beam Irradiation », *J. Spacecr. Rockets*, **vol. 53**, no 6, p. 1100-1104, 2016.

- [28] R. Hoffmann and J. R. Dennison, « Measurement Methods of Electron Emission Over a Full Range of Sample Charging », *IEEE Trans. Plasma Sci.*, **vol. 40**, no 2, p. 298-304, 2012.
- [29] A. E. Jensen and J. R. Dennison, « Defects Density of States Model of Cathodoluminescent Intensity and Spectra of Disordered SiO<sub>2</sub> », *IEEE Tran. Plasma Science*, **vol. 43**, n°9, p. 2925-2932, 2015
- [30] J. Garcia-Guinea et Al., « Luminescence of  $\alpha$ -Al<sub>2</sub>O<sub>3</sub> and  $\alpha$ -AlOOH natural mixtures », *Radiat. Meas.*, **vol. 33**, no 5, p. 653-658, 2001.
- [31] A. R. N. Kristianpoller, « Radiation effects in pure and doped Al<sub>2</sub>O<sub>3</sub> crystals », *Nucl. Instrum. Amp Methods Phys. Res. Sect. B-Beam Interact. Mater. At.*, **vol. 141**, no 1, p. 343-346, 1998.
- [32] R. C. Powell, B. DiBartolo, B. Birang, and C. S. Naiman, « Fluorescence studies of energy transfer between single and pair Cr<sup>3+</sup> systems in Al<sub>2</sub>O<sub>3</sub> », *Phys. Rev.*, **vol. 155**, no 2, p. 296, 1967.
- [33] B. A. Green and B. C. Passenheim, « Broad-band radioluminescence in electron-irradiated ionic compounds », *J. Appl. Phys.*, **vol. 48**, no 1, p. 424, 1977.
- [34] P. Jonnard, C. Bonnelle, G. Blaise, G. Rémond, and C. Roques-Carmes, « F<sup>+</sup> and F centers in  $\alpha$ -Al<sub>2</sub>O<sub>3</sub> by electron-induced x-ray emission spectroscopy and cathodoluminescence », *J. Appl. Phys.*, **vol. 88**, no 11, p. 6413-6417, 2000.
- [35] M. J. Springis and J. A. Valbis, « Red Luminescence of Color Centres in Sapphire », *Phys. Status Solidi B*, **vol. 132**, no 1, p. K61-K65, 1985.
- [36] R.C. Powell, « The Interaction of Chromium Ions in Ruby Crystals ». PhD Thesis, Arizona State Univ., 1967.
- [37] M. Ghamnia, C. Jardin, et M. Bouslama, « Luminescent centres F and F<sup>+</sup> in  $\alpha$ -alumina detected by cathodoluminescence technique », *J. Electron Spectrosc. Relat. Phenom.*, **vol. 133**, n° 1-3, p. 55-63, 2003.